



Cite this: *Mater. Adv.*, 2024,  
5, 1998

# PVA/guanidinium oleate transdermal patch as a pH-responsive drug delivery system for the localized and targeted delivery of anticancer drugs†

Monika Jain, <sup>‡a</sup> Raviraj Pansuriya,<sup>a</sup> Rahul Thakur,<sup>b</sup> Adesh K. Saini,<sup>b</sup> Sugam Kumar, <sup>c</sup> Vinod K. Aswal, <sup>c</sup> Suresh Kumar Kailasa <sup>a</sup> and Naved I. Malek <sup>‡a</sup>

The exponential growth in the development of biocompatible patch-type drug delivery as an alternative to traditional intravenous or subcutaneous injections is because it can be applied to patients with needle phobia and can overcome the need for highly trained personnel. Through a patch, a drug can be administered locally, ensuring relief from side effects and the regulated distribution of the drug to the site of action. Keeping in mind the relevance of mucoadhesive polymers (e.g. polyvinyl alcohol, PVA) in site-specific drug delivery, an attempt was undertaken in the current study to create a mucoadhesive patch of PVA through mixing it with a pH-responsive surface-active ionic liquid (guanidinium oleate, [Gu][Ol]). The patch was studied for its pH-responsiveness, mechanical qualities, adhesive properties, stretchability, and self-healing properties. The studied mucoadhesive patch was further used to load and deliver anticancer medication 5-fluorouracil (5-FU) through transdermal delivery at pH 7.2. The drug-release profiles of the transdermal patch revealed that up to 60% of the adsorbed medication was released in 48 hours at pH 7.2. The results demonstrate that the designed transdermal mucoadhesive patch is a potent pH-responsive vehicle for targeted and localized drug delivery.

Received 30th June 2023,  
Accepted 6th January 2024

DOI: 10.1039/d3ma00346a

rsc.li/materials-advances

## 1. Introduction

Recent research on transdermal drug-delivery systems (TDDSs) for targeted chemotherapeutic distribution has demonstrated their advantages such as bypassing liver metabolism and minimizing side effects.<sup>1–8</sup> TDDSs are proven to be beneficial for treating localized tumours, such as breast and skin malignancies, enabling prolonged low-dose treatments with minimal side effects. An intricate challenge arises with hydrophilic and high molecular weight drugs, such as 5-fluorouracil (5-FU), doxorubicin (DOX), and proteins, as the formidable stratum corneum (SC) barrier resists their permeation as a result of its

robust hydrophobic nature.<sup>9–12</sup> To address this limitation, traditional chemical enhancers such as ethanol, sulfoxide, azone, and terpenoids have been explored; however, safety concerns as well as toxicity and skin irritation issues persist, emphasizing the need for innovative solutions in transdermal drug delivery.<sup>13–16</sup> Recently, ionic liquids (ILs) have attracted attention owing to their tunable physico-chemical characteristics and environment-friendly nature.

Because of their unique tunable character, several ILs have been specially designed and explored as transdermal chemical enhancers with an aim to improve the transdermal delivery of drug molecules through the SC layer of the skin.<sup>17</sup> Specifically, [C<sub>12</sub>dabco][Br] (*N*-dodecyl-dabco bromide), [C<sub>6</sub>C<sub>6</sub>dabco][Br] (*N,N*-di-hexyl-dabco bromide), [C<sub>12</sub>Mim][Tf<sub>2</sub>N] (1-dodecyl-3-methylimidazolium bis(trifluoromethyl sulfonyl)-amide), and [C<sub>1</sub>C<sub>4</sub>SO<sub>3</sub>Hpyrr][HSO<sub>4</sub>] (*N*-methyl-*N*-(4-butylsulfonic acid) pyrrolidinium hydrogen sulfate) have potentially enhanced skin permeation of drugs owing to the presence of anionic hydrophobic groups that can reduce the skin barrier function.<sup>18,19</sup> Though these ILs have been proposed as a replacement to conventional chemical penetration enhancers, there are persistent concerns regarding their toxicity, biocompatibility, and poor biodegradability because of the presence of pyridine- or

<sup>a</sup> Ionic Liquids Research Laboratory, Department of Chemistry, Sardar Vallabhbhai National Institute of Technology, Surat-395007, Gujarat, India.  
E-mail: navedmalek@chem.svnit.ac.in

<sup>b</sup> Department of Biotechnology, Central Research Laboratory, MMES, Maharishi Markandeshwar University, Mullana, Haryana-133 207, India

<sup>c</sup> Solid State Physics Division, Bhabha Atomic Research Centre, Trombay, Mumbai-400085, India

† Electronic supplementary information (ESI) available: Synthesis and characterization of [Gu][Ol] and its surface-active properties. See DOI: <https://doi.org/10.1039/d3ma00346a>

‡ MJ and RP share the equal contribution.

imidazolium-based cations and hexafluorophosphate- or tetrafluoroborate-based anions.<sup>20</sup> To overcome these limitations, attention has been focused on the development of ILs with a biocompatible, biodegradable character and negligible toxicity, such as ILs made from cations such as choline, guanidine, and functionalized amino acids in combination with anions such as fatty acids (e.g. oleate, linoleate, and palmitate).<sup>21–23</sup> These pH-responsive ILs have shown promise for targeted anticancer drug delivery owing to the pH gradient between the tumour and normal tissues; however, detailed exploration of pH-responsive ILs with skin-permeation characteristics is still lacking.<sup>24–30</sup> However, the pH-dependent skin permeation of the anticancer drug imiquimod was investigated using nanostructures made of ILs based on guanidinium-fatty acids,<sup>27</sup> while in another study the solubility and transdermal delivery of ibuprofen and peptide drugs were enhanced through fatty acid-based ILs.<sup>31</sup> Also, a choline-amino acid IL-based system was studied for the improved permeation of acyclovir through the skin,<sup>32</sup> while choline oleate ([Ch][Ol])-based vesicular aggregates were explored recently by our group as a new-age drug-delivery vehicle for the targeted delivery of doxorubicin.<sup>33</sup> [Ch][Ol] was also explored by Goto *et al.* to enhance skin permeability.<sup>32</sup>

Among the studied TDDSs, such as microemulsions, micelles, vesicles, nanoparticles, and transdermal patches,<sup>37–43</sup> transdermal patches are preferred because of their multi-responsiveness with high water retention capacity, robust mechanical properties, self-healing capacity, adhesiveness, and reusability.<sup>44–47</sup> Moreover, the utilization of transdermal patches in drug-delivery systems holds promise for enhancing drug penetration and also facilitating a sustained release of therapeutic agents. This approach offers a more straightforward and convenient application method, potentially leading to improved treatment effectiveness and enhanced patient adherence.<sup>44</sup>

In the present work, we designed pH-responsive guanidinium oleate ([Gu][Ol])-based transdermal patches through an interaction with polyvinyl alcohol (PVA) and using borax as a cross-linker, and used this system to deliver the hydrophilic chemotherapeutic drug 5-FU. The reason behind replacing choline with guanidinium cation was due to the stability of the guanidinium cation over the desirable pH range and its extensive H-bonding capacity with six H-bond donor sites. The planar resonating structure of the guanidinium cation with evenly distributed positive charges among the three nitrogens is responsible for its increased electrostatic interactions and strength of H-bonds it forms.<sup>34</sup> These enhanced interactions with biological barriers, such as the SC, cell membrane, and outer membrane of microbes, distinguish guanidinium as a suitable transporter or vector for macromolecules through these barriers.<sup>35</sup> Looking at the highest skin permeation enhancement ratio for oleic acid,<sup>36</sup> we believed that a pH-responsive intelligent [Gu][Ol]-based transdermal patch could deliver the hydrophilic chemotherapeutic drug 5-FU through penetrating the SC layer.<sup>47–49</sup> The developed patch was characterized by various methods, such as SANS, FT-IR, SEM, and rheological analysis. The adhesiveness, self-healing properties, and effect of pH as well as temperature stimuli on the system

were also studied in detail. Further, the *in vitro* permeation of 5-FU was investigated by Farzan diffusion cells on goat skin. The *in vitro* biocompatibility of the system was investigated on a normal human cell HaCaT cell line and the *in vitro* cytotoxicity of the 5-FU-loaded patch was studied on a breast cancer cell line (MCF-7 cells). The reported system paves the way for new-age intelligent drug-delivery vehicles for targeted and localized drug delivery.

## 2. Experimental section

### 2.1. Materials

Poly(vinyl alcohol) (PVA) and sodium tetraborate (99.98%) were purchased from Sigma and used as received. Guanidinium oleate ([Gu][Ol]) was synthesized and characterized as per previous reported methods.<sup>50,51</sup> 5-Fluorouracil (5-FU) (> 99.0%) was purchased from TCI and used as received. The structures of the chemicals used in the present study are given in Scheme 1.

### 2.2. Preparation of the transdermal patch

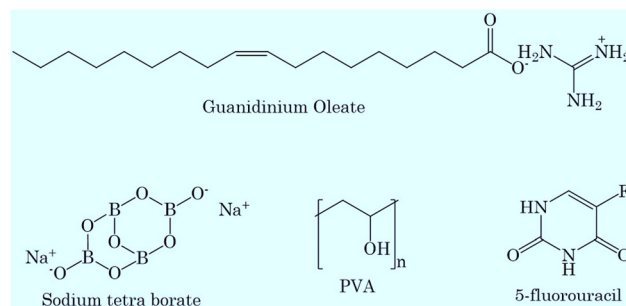
To prepare the transdermal patch, in an aqueous solution of [Gu][Ol] (15 mM), 10 wt% PVA was added while stirring. The mixture was then heated up to 60 °C to dissolve the PVA. To this homogeneous transparent solution (5 ml) (in heated state), a 1 ml (0.04 M) aqueous solution of borax was added. The solution was again heated up to 60 °C and the resulting homogeneous transparent solution was poured in to a Petri dish, then placed at room temperature. The solution was allowed to naturally cool and dry at room temperature for 24 hours to get the final patch. A schematic representation of the process is given in Scheme 2.

### 2.3. Fourier-transform infrared spectroscopy (FTIR)

A Shimadzu FTIR-8400S spectrophotometer was used to record the FTIR spectra of [Gu][Ol] aqueous solution and PVA + [Gu][Ol] + sodium tetraborate + H<sub>2</sub>O to determine the possible interactions of [Gu][Ol] with PVA and sodium tetraborate.

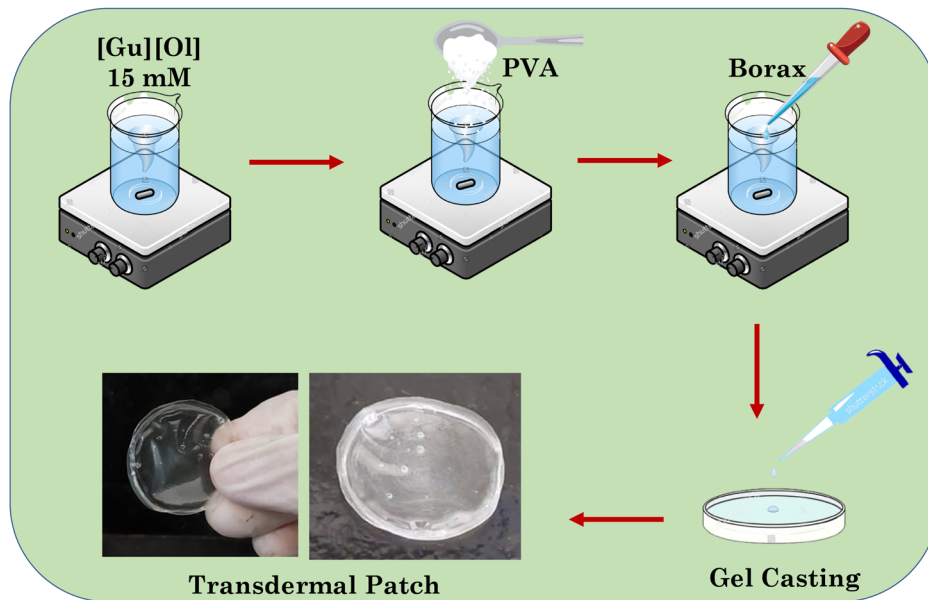
### 2.4. Small-angle neutron scattering (SANS)

The SANS experiments were performed by the SANS diffractometer at the Guide Tube Laboratory, Dhruva Reactor, BARC, Mumbai, India. The coherent differential scattering cross-section ( $d\Sigma/d\Omega$ ) per unit volume was measured as a function of the wave-vector transfer  $q = 4\pi\sin\theta/\lambda$ , where  $\lambda$  is the



Scheme 1 Structures of the chemicals used.





**Scheme 2** Schematic representation showing the preparation of the transdermal patch.

wavelength of the incident neutrons and  $2\theta$  is the scattering angle. The wavelength of the incident monochromatized beam from the neutron velocity selector was  $5.2 \text{ \AA}$  with a dispersion of  $\Delta\lambda/\lambda \sim 15\%$ . The angular distribution of dispersed neutrons was recorded through a 1 m long one-dimensional  $\text{He}^3$  position-sensitive detector. The  $q$ -range of the instrument was  $0.017\text{--}0.35 \text{ \AA}^{-1}$ . All of the measurements were carried out at a constant temperature of  $30^\circ\text{C}$ . The scattering data were fitted through SAS Fit analysis software using different fitting models.

## 2.5. Morphology of the hydrogel

The morphology of the prepared transdermal patch was studied by SEM (Hitachi S-3400 N). After drying in the ambient atmosphere and coating with gold, the biofilm was examined with a Hitachi S-3400N scanning electron microscope at 15 kV.

## 2.6. Mechanical properties obtained through rheology measurements

To analyse the mechanical properties of the patch, rheological experiments were carried out using Anton Paar Physica MCR 301 rheometer. To confirm the viscoelastic nature of the transdermal patch, angular frequency sweep measurements ( $1\text{--}1000 \text{ rad s}^{-1}$ ) were performed at  $25^\circ\text{C}$ , at a constant strain of 0.1% using a parallel plate with a 40 mm diameter and default gap of 1 mm that was attached to a transducer. To confirm the elastic property of the patch, the measurements were performed within the viscoelastic region where  $G'$  (storage modulus) and  $G''$  (loss modulus) are independent of strain. To analyse the strain-bearing capacity of the patch, strain sweep measurements were performed at a constant frequency of  $5 \text{ rad s}^{-1}$  for a range of strain from 1%–1000%. To analyse the temperature effect on the viscoelastic property of the gel, temperature sweep measurements were performed at a constant frequency ( $5 \text{ rad s}^{-1}$ ) and constant strain (0.1%).

## 2.7. pH-dependent dynamic swelling behaviour

To investigate the swelling behaviour of the film at two different pH levels (7.4 and 5), two accurately weighed pieces of films were submerged in separate containers of 10 ml aqueous PBS buffer solutions at pH 7 and pH 5 at  $37^\circ\text{C}$ . At fixed time intervals, the samples were removed from the medium and weighed after drying with tissue paper. To evaluate the swelling ratio of the patch, eqn (1) was applied to the collected data:

$$Q = \frac{W_a}{W_b} \quad (1)$$

where  $W_a$  is the weight of water molecules in the swollen 3D network of the patch and  $W_b$  is the weight of the dry gel.

## 2.8. Phase transition as a function of temperature

The transition of the patch from opaque to transparent was studied through measuring the turbidity of the system. The turbidity was measured in terms of the % transmittance (% T) through using a UV-visible spectrophotometer. The % T was measured at a wavelength of 500 nm, because at this wavelength none of the components from the system gives any absorption peak.

## 2.9. Drug loading

We used a modified breathing-in method to load the 5-FU into the patch. In summary, a known-weight patch was placed in a dialysis bag and immersed in a known-concentration of 5-FU. A UV-Vis spectrophotometer set at 250–350 nm was used to calculate the percentage of encapsulation in the patch after a given period of time through determination of the drug concentration left in the drug solution. The drug-loaded biofilm was again freeze-dried. The loading efficiency (LE%) and the encapsulation efficiency (EE%) were calculated using the following



equations:

LE %

$$= \frac{\text{initial drug concentration} - \text{drug concentration after loading}}{\text{initial drug concentration}}$$

$\times 100$

(2)

EE %

$$= \frac{\text{loading efficiency} - \text{initial drug concentration } (\mu\text{g ml}^{-1})}{\text{initial concentration}}$$

$\times 100$

(3)

### 2.10. Stratum corneum (SC) studies using FTIR

In order to conduct FTIR examinations of the SC, the goat skin was treated as stated previously.<sup>36</sup> The entire thickness of the goat skin was thawed at room temperature from the freezer for 1 h. After that, the skin's fat layers were removed, and the SC was separated from the skin by heating it for 10 min over aluminium foil on a hot plate (60 °C). The SC was then immersed in 1% trypsin solution for 24 hours to break down any attached skin tissue. Then the SC was rinsed three times with water and dried at room temperature in a fume hood.

Then the treated SC was cut into 1.5 cm  $\times$  1.5 cm pieces and incubated at 32.5 °C for 24 hours with 3 mg of test material to see how the resulting gel influenced the skin barrier characteristics. Finally, the SC samples were washed in 20% ethanol solution and dried at ambient temperature for 24 hours before recording the FTIR spectra for the SC without and with immersion in the sample within the range of 500–4000 cm<sup>−1</sup> with 20 scans.

### 2.11. Skin-penetration study

A Franz diffusion cell was used to conduct the skin-permeation tests. The fat layer of the skin was scraped away carefully, and the skin was cut into 1.5  $\times$  1.5 cm<sup>−1</sup> pieces. The skin was put into the Franz diffusion cell with the inner skin in the receptor phase. The receptor phase, *i.e.* 10 ml phosphate buffer solution, was constantly agitated at 32.5 °C. After that, 500 mg of the patch was drawn on the outer side of the skin (donor compartment) and covered with parafilm to reduce contamination. Aliquots of 0.1 ml from the receiving compartment were taken at regular intervals for 48 hours. These aliquots were analysed through UV-Vis spectroscopy for determination of the concentration of 5-FU released at different time intervals.

### 2.12. Cytotoxicity evaluation

The 3-(4,5-dimethylthiazol-2-yl)-2,5-diphenyltetrazolium bromide (MTT) assay was used to measure the *in vitro* cytotoxicity. An Eppendorf cellXpert@C170 incubator was used to incubate the HaCaT (human keratinocyte cell line) and MCF-07 (human breast cancer cell line) cells under humidified conditions at 37 °C and 5% CO<sub>2</sub>. The cells were cultured in 10% complete medium (foetal bovine serum + Dulbecco's minimal necessary

media) and were then chosen. Each well of a 12-well plate was seeded with roughly 1  $\times$  10<sup>5</sup> cells, which were then exposed to 200 mg of test system in the culture media. The well plate was then incubated again under the aforementioned conditions for 24 hours and 48 hours, respectively. The cells were then carefully rinsed in PBS buffer and again incubated with MTT solution for 4 hours and dissolved in 200  $\mu$ l DMSO per well. Using an Epoch multiplate reader, the absorbance at 570 nm was measured after 10 min. Calculations of the cell viability were made in relation to both the positive and negative controls.

## 3. Results and discussion

Here, we aimed to develop an intelligent transdermal drug-delivery patch that could be programmed to administer medication by penetrating the skin and releasing it mostly at an acidic pH. Currently, PVA films are used as transdermal drug-delivery vehicles,<sup>52</sup> but they have poor elastic properties, low hydrophilicity, and limited skin permeability. To enhance the elastic properties and to incorporate a self-healing property in the PVA-based patch, we added borax. Following the addition of the borax solution, the PVA solution was crosslinked by the borate anions and the hydroxyl groups on the PVA backbone, forming boric ester linkages that resulted in the formation of a 3D network for the hydrogel, as confirmed by the FTIR results *vide infra*. The borax–PVA hydrogel structures could be easily recovered, demonstrating the dynamic reversibility of the hydrogen bonds and boric ester bonds within the 3D structure.<sup>53</sup> To incorporate a pH-responsive drug-release characteristic and to enhance the skin permeation of the encapsulated drug, we added [Gu][Ol] as an additive. [Gu][Ol], being a salt of guanidinium and oleic acid, has a pH-responsive characteristic and can also improve the permeation of medication through skin. Specifically, the guanidinium cation carries high basicity that remains protonated over a wide pH range. Also, the planar structure with H-bonding sites of the guanidinium cation is responsible for H-bonding and electrostatic interactions that further help to form self-assembled nanoaggregates. Guanidinium ions exhibit binding towards phosphate and carboxylate groups, hence DNA and RNA binding proteins show affinity towards guanidinium ions.<sup>34</sup> Guanidinium ions can also interact with the lipophilic anions of the cell membrane to facilitate translocation through lipophilic membranes or cell membranes.<sup>54</sup> Hence guanidium-containing compounds can serve as a transporter not only for a typically water soluble moiety but also for macromolecules such as proteins and nucleic acids through the cell membrane and SC as well.<sup>35</sup> The anion of the surface-active ionic liquid (SAIL) used in the present investigation was oleic acid, which is a known permeation enhancer.<sup>36,55</sup> Here, we used the SAIL beyond its cmc (Table S1 and Fig. S2, ESI<sup>†</sup>), in order to use the self-assembled nanoaggregates of [Gu][Ol]. These nanoaggregates, through interacting with the 3D coils of the aggregated gel of PVA and borax, could form the transdermal patch, in which the drug molecules are encapsulated inside these nanoaggregates,



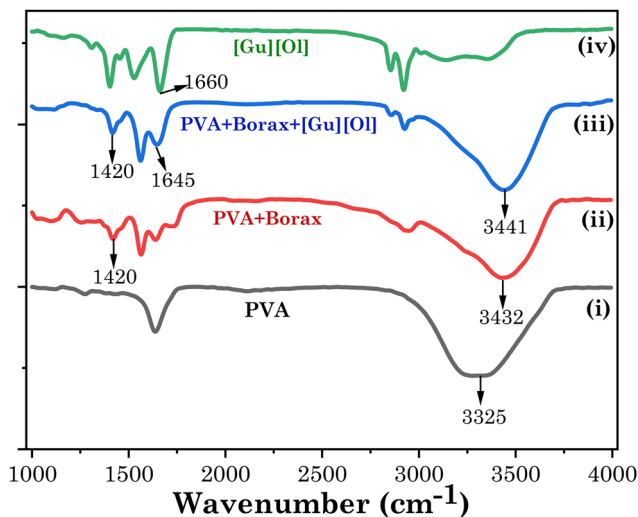


Fig. 1 FTIR spectra of (i) PVA (black), (ii) PVA + borax (red), (iii) PVA + borax + [Gu][OI] (blue), and (iv) [Gu][OI] (green).

as confirmed by the SANS results *vide infra*. These self-assemblies of the SAIL are unstable at acidic pH, as the SAIL itself is pH-responsive.<sup>27</sup> Hence at lower pH, the self-assemblies of the SAIL rupture and the drug is released faster compared to at neutral pH, as confirmed by the drug permeation study through goat skin at pH 7.4 and pH 5.2, *vide infra*.

To consider the patch for drug delivery, it was of prime importance to study the interactions that prevail within the system. To investigate the interactions within the present system, the FTIR spectra of neat [Gu][OI], neat PVA, PVA + borax patch, and the transdermal patch (PVA + borax + [Gu][OI]) were obtained and compared. As demonstrated in Fig. 1, there was no peak at 1420 cm<sup>-1</sup> for PVA alone, but the PVA + borax spectrum displayed an additional peak at 1420 cm<sup>-1</sup>. Rezvan *et al.* demonstrated that the additional peak at 1420 cm<sup>-1</sup> indicated the formation of PVA-borate bonds.<sup>18</sup> Hence after the addition of borax, a PVA-borate complex was formed, which was also stable even after the addition of [Gu][OI] as that peak still existed in the PVA + borax + [Gu][OI] system. The -OH peak of PVA at 3325 cm<sup>-1</sup> was shifted towards higher frequency after the addition of borax to 3432 cm<sup>-1</sup>, indicating the breakdown of the intramolecular H-bonds of PVA because of the formation of the PVA-borate complex. Further, after the addition of [Gu][OI], the -OH peak of PVA was slightly more shifted towards higher frequency, *i.e.* to 3441 cm<sup>-1</sup>, which was because of the breaking of the intramolecular H-bonds of PVA and the formation of intermolecular H-bonds between the -OH of PVA and -COO of oleate. This was also proved through the decrease in the stretching frequency of the -C=O of oleate from 1660 cm<sup>-1</sup> to 1645 cm<sup>-1</sup>.<sup>53</sup>

To investigate the shape and size of the self-assembled nanostructures present in the system, the small-angle neutron scattering (SANS) measurements were performed. In SANS measurements, the intensity of the scattered neutrons are measured, which is proportional to the  $d\Sigma/d\Omega$ , *i.e.* the differential scattering cross-section per unit volume as a function of

the wave-vector transfer ( $q$ ). The measured data were then fitted using SASfit software employing different suitable models. Shibaev *et al.* also did the same SANS study for a PVA + borax gel system and the data were well fitted by the generalized Ornstein-Zernike model, thereby describing scattering from polymer gels.<sup>54,56</sup> Following a similar protocol, we also employed the following Ornstein-Zernike equation to model the scattering from the PVA + borax gel:

$$I(q) = \frac{I_{OZ}(0)}{[1 + (q\xi)^2]} \quad (4)$$

where  $I(0)$  is the forward scattering and  $\xi$  is the correlation length, describing the space where excluded volume effects are present. The correlation length of the PVA + borax gel system was found to be around 6.9 nm.

In the case of the PVA + borax + [Gu][OI] gel (Fig. 2(a)), the scattering intensity at higher  $q$  values was similar to that of the PVA + borax gel; however, a significant increase in the low  $q$  scattering was observed (Fig. 2(b)). To account for this contribution in the low  $q$  region, we included one more term in eqn (4), consistent with the traditional two-stage model of the polymer gel:<sup>54-57</sup>

$$I(q) = \frac{I_{OZ}(0)}{(1 + Q^2\xi^2)} + \frac{I_{DB}(0)}{(1 + Q^2\xi^2)^2} \quad (5)$$

The second term in eqn (5) is the Debye-Bueche function and is usually employed to account for the scattering from larger solid-like inhomogeneities in a sample, contributing to the scattering in the low  $q$  region. Here,  $\xi$  represents the characteristic size of these inhomogeneities.

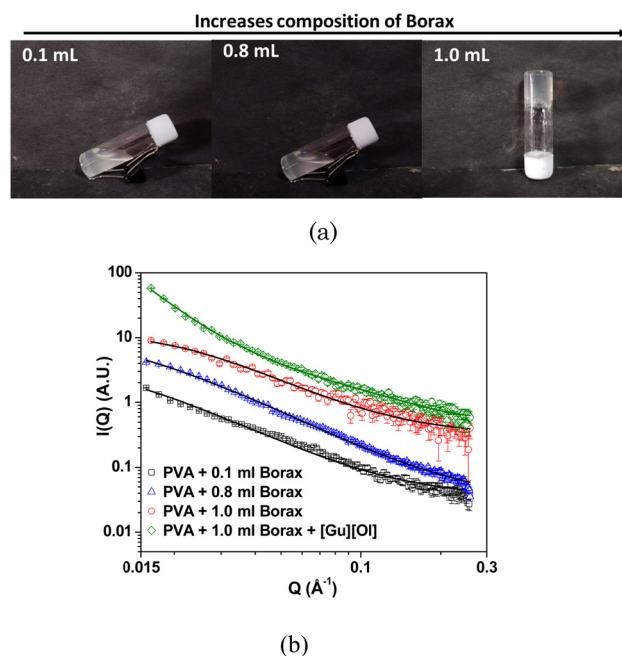


Fig. 2 (a) Visual images of PVA gel with varying concentrations of borax, (b) SANS data of the PVA gel with varying concentrations of borax and the PVA + borax + [Gu][OI] system. The data are shifted vertically for clarity in the presentation.



Since no low  $q$  cut-off was observed in the scattering data, we modified eqn (5) by replacing the second term by a simple power law:

$$I(Q) = \frac{I_{0z}(0)}{(1 + Q^2\xi^2)} + \frac{I_1}{Q^{-n}} \quad (6)$$

where  $I_1$  is a  $Q$  independent proportionality constant and  $n$  is the Porod exponent, providing information about the fractal nature of the gel.

As the concentration of borax increased in the system, the correlation length also increased, suggesting an enhanced cross-linking in the polymer. The correlation length of the PVA + borax + [Gu][Ol] system was found to be 3.7 nm, which was significantly less than that of the PVA + borax gel (Table 1). This could be attributed to the presence of aggregates of [Gu][Ol] within the gel network, increasing the cross-linking and hence decreasing the correlation length. Moreover, the value of  $n$  was found to be nearly 2.9, which suggested a densely packed gel structure.

The morphology of the transdermal patch was investigated through SEM. As shown in the SEM images of the transdermal patch, there was a 3D network of thread-like fibres (Fig. 3(a) and (b)). These thread-like fibres demonstrated the network of 3D coils of PVA. These coils were connected through hydrogen bonds and boric ester linkages between PVA and borax.<sup>53</sup> The self-assembled structures of [Gu][Ol] associated within the 3D network were visible at 50 000 times magnification (Fig. 3(b)). As shown in Fig. 3(c), quantitative analysis of the fibres present in the patch was done by ImageJ software. According to this study, the minimum and maximum lengths of the fibres were 112  $\mu\text{m}$  and 552  $\mu\text{m}$ , respectively. The average length of the fibres was 251  $\mu\text{m}$ .

To qualify as a drug-delivery system, it was of prime importance to know the mechanical properties of the patch. Here, we used rheological measurements (angular frequency sweep and strain sweep) to investigate the mechanical strength of the transdermal patch. In the system, borax was used as a cross-linker to enhance the mechanical properties of the system. At a lower composition of borax (0.5 mL, 0.004 M), the system was in a sol form. Here, the loss modulus ( $G''$ ) was greater than the storage modulus ( $G'$ ), as shown in Fig. 4(a) and (b) for the frequency sweep test and strain sweep test, respectively, indicating the system was in a sol form, and the hydrogel was not formed. The 3D network was formed at a borax composition of 1 mL (0.004 M). At this composition, the frequency sweep rheogram (Fig. 4(c)) showed that the storage modulus ( $G'$ ) was higher than the loss modulus ( $G''$ ), demonstrating that

the elastic component was dominant over the viscous component. This indicates the rigid gel-like structure of the test material.<sup>57</sup> With rising angular frequency, the storage modulus ( $G'$ ) and loss modulus ( $G''$ ) both initially rose, becoming frequency-independent at higher frequencies. The dynamic response shown here was typical of gel-like materials.<sup>58,59</sup>

As demonstrated in the strain sweep rheogram (Fig. 4(d)), at up to 1000% strain,  $G'$  was greater than  $G''$ , indicating the elastic component was greater than the viscous component. The test material exhibited more solid-like characteristics below 1000% strain. At and above 1000% strain, the material exhibited a dominating viscous component over the elastic component, as shown by  $G'$  being lower than  $G''$ . This strain is known as the critical strain, above which a material behaves like a liquid.

As demonstrated in the temperature sweep rheogram (Fig. 4(e)), with the increase in temperature, the loss modulus ( $G''$ ) also increased, demonstrating the increasing viscous component, and indicating the conversion of the gel to a sol. At 55  $^\circ\text{C}$  temperature, there was a crossover point for the storage modulus and loss modulus, known as the gel point. Above this temperature, the material exhibited a more liquid-like property. Above the gel point, the decrease in elastic component (storage modulus) indicated the deformation of the 3D network of the gel, leading to a transition to the viscous sol form.

We also explored the self-healing property of the designed transdermal patch. For this, we cut the patch into fragments before complete drying. We then put those fragments in contact with each other. As demonstrated in the visual images in Fig. 5(a), without any external stimuli (under ambient temperature), these fragments rebuilt as a whole patch before we cut again into fragments, which were smoother without any mark of breakage after the self-healing. Further, we measured the time for self-healing at various distances (Fig. 5(b)). As the distance between the hydrogel increased, the time for self-healing also increased. For successive distances of 0.2, 0.5, and 0.9 cm between two pieces of hydrogel, the self-healing times were 1.12, 3.21, and 6.55 min, respectively. Beyond a distance of 0.9 cm between the hydrogel, self-healing did not occur.

We also analysed the self-healing property of the hydrogel through relaxation tests. For this, we measured the viscosity of the hydrogel as a function of time at two different angular frequencies (1  $\text{rad s}^{-1}$  and 100  $\text{rad s}^{-1}$ ). The hydrogel kept at the 1  $\text{rad s}^{-1}$  angular frequency for 50 s remained in the gel form. As the angular frequency increased to 100  $\text{rad s}^{-1}$ , the hydrogel was converted to its sol form, as demonstrated in Fig. 5(c), and the viscosity drastically decreased. As the angular frequency again decreased for 50 s, up to 1  $\text{rad s}^{-1}$ , the hydrogel again reformed to the gel form, exhibiting high viscosity. It took 50 s for the hydrogel to self-heal.

As we designed a transdermal drug-delivery patch here, it was essential to study the adhesive property of the test material with the hydrogel (Fig. 6(a)). We successfully explored the adhesive property of the patch through lap shear tests with skin, rubber, and steel. For that a 10 mm contact area of substrate (skin, rubber, or steel) was stuck on the patch and stretched at a regulated pace of 100  $\text{mm min}^{-1}$  while the

**Table 1** Fitted correlation lengths for the SANS data of the PVA gel samples

Sample	Correlation length (nm)
PVA + 0.1 ml Borax	8.5
PVA + 0.6 ml Borax	7.7
PVA + 1.0 ml Borax	6.9
PVA + Borax + [Gu][Ol]	3.7



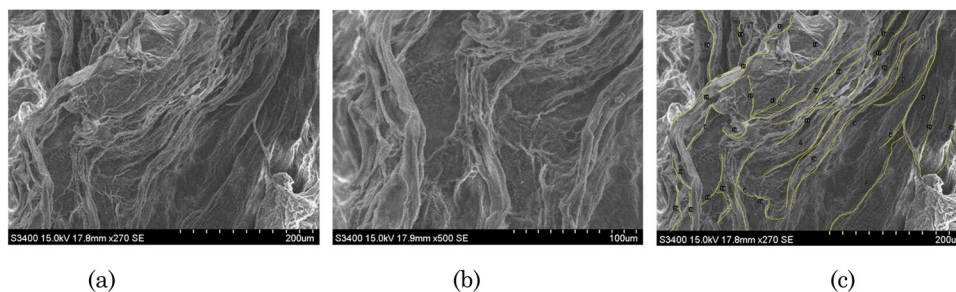


Fig. 3 (a) and (b) SEM images of the transdermal patch; (c) qualitative analysis of the patch by ImageJ.

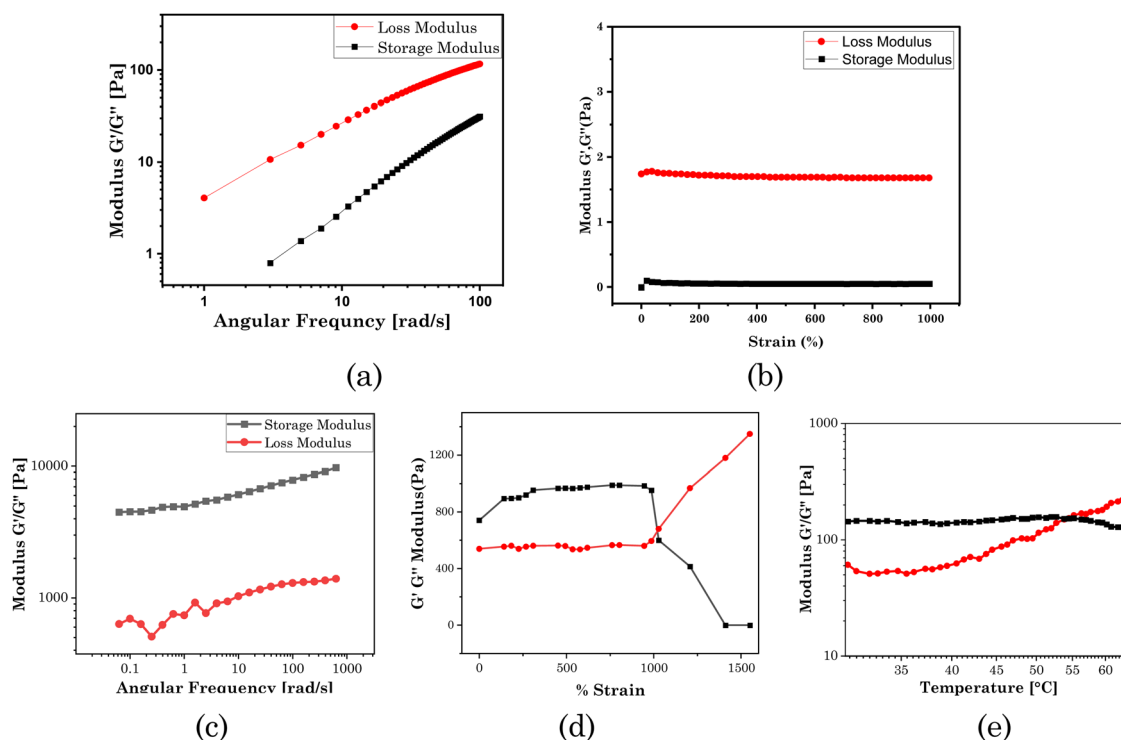


Fig. 4 Rheological analysis of a borax composition of 0.5 ml in the system (0.004 M): (a) frequency sweep test, (b) strain sweep test; and of a borax composition of 1.0 ml (0.004 M) in the system: (c) frequency sweep rheogram, (d) strain sweep rheogram, and (e) temperature sweep rheogram.

substrate remained stable. The results are presented in the form of a plot between the adhesion stress and displacement in Fig. 6(b). The patch exhibited the maximum adhesion with rubber and minimum with steel, as per their surface roughness (Table 2). Hence the prepared transdermal patch displayed significant adhesive strength with skin (6.95 kPa), which was greater than the adhesive strength of the PVA-based ionic hydrogel (5.22 kPa)<sup>60</sup> and suggests it can be used as a suitable transdermal drug-delivery patch.

The stretchability of the test material was also explored, as demonstrated in Fig. 7(a), showing that the material could be stretched up to 4 times its length. We also measured the toughness using the as-prepared sample patch and a notched patch (see the graphical representation in Fig. 7(b) and (c)). The results are demonstrated in the form of a plot between the stress and stretch in Fig. 7(d). The sample with an edge cut was

easier to stretch to fracture, and its critical stretch ( $\lambda_{\text{critical}}$ ) value, *i.e.* 19.4, was lower than the  $\lambda_{\text{critical}}$  of the unnotched sample, *i.e.* 23.3.

The toughness of the hydrogel or load-bearing capacity were also estimated, as shown in Fig. 8. A weight loading of 0.150 kg could be supported by the hydrogel film, but damage was seen at the cut site when the force applied was over its limit (0.250 kg), with the photos demonstrating the hydrogel film's exceptional toughness shown in Fig. 8. We also computed the relative strength (RS), or the ratio of the hydrogel film's loaded weight to its weight, to corroborate these statistics. In the current cases, the projected values of RS for loaded weights of 50, 100, and 150 were 833, 1667, and 2500, respectively.

We evaluated the wettability of the patch and the effect of pH by observing the swelling kinetics of the transdermal patch in an aqueous PBS medium of pH 7 and 5. The results are shown in Fig. 9(a). The fibrous 3D network structure of the



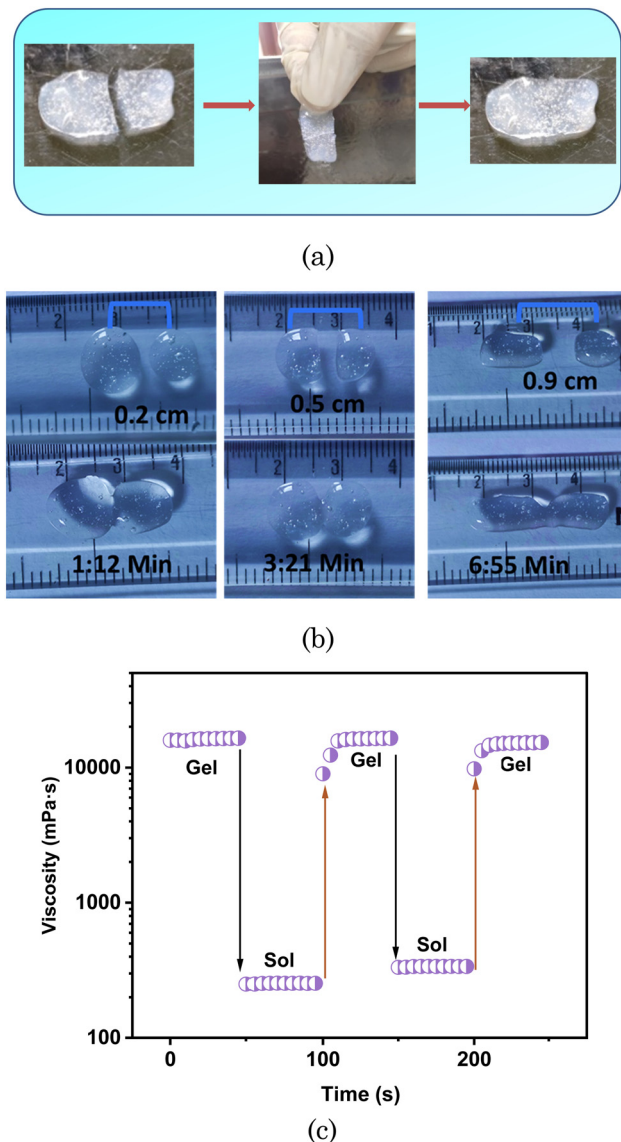


Fig. 5 (a) Visual images demonstrating the self-healing property of the transdermal patch. (b) Self-healing of the hydrogel at different distances. (c) Relaxation test of the hydrogel, and viscosity of the hydrogel at a low angular frequency of  $1 \text{ rad s}^{-1}$  for 50 s, and a high angular frequency of  $100 \text{ rad s}^{-1}$  for 50 s.

patch allowed it to quickly absorb water when submerged in aqueous PBS. According to the results, a perfectly dried patch immersed in a PBS buffer of neutral pH (pH 7) could absorb water up to four times its weight and reached a fully saturated condition in around  $70 \pm 5 \text{ min}$ . However, when immersed in acidic PBS buffer (pH 5), it could only absorb water twice as much as its weight, occurring in  $20 \pm 5 \text{ min}$ , and after that it began to degrade. This was because at this pH the added SAIL ([Gu][Ol]) was not stable, which we confirmed through changing the pH of solution of [Gu][Ol] in water. At neutral pH, a clear solution in water was obtained, then as the pH decreased up to 5, the solution turned highly turbid (Fig. 9(b)). Hence the addition of [Gu][Ol] in the transdermal patch endowed it with pH-responsive properties, thus constituting an intelligent pH-

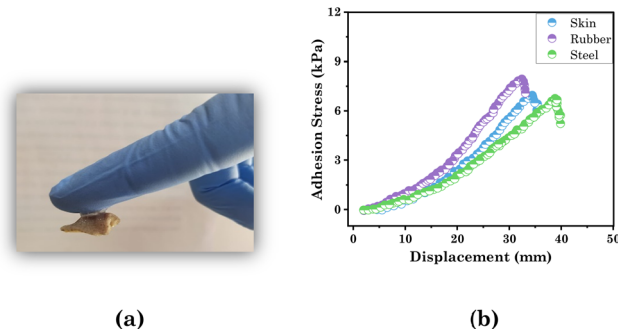


Fig. 6 Visual images demonstrating (a) adhesive property with skin and (b) lap shear test of the hydrogel for assessing the adhesion strength with skin, rubber, and steel.

Table 2 Adhesion strength of the hydrogel with different materials

Materials	Adhesion strength (kPa)
Skin	6.95
Rubber	7.94
Steel	6.75

responsive transdermal drug delivery system, which could release the carried drug specifically in an environment with an acidic pH.

Fig. 10 illustrates the phase transition of the system from opaque to transparent and then gel to sol as a function of temperature. At temperatures below  $20^\circ\text{C}$ , the patch was opaque, and then as the temperature increased it turned to transparent at and above  $40^\circ\text{C}$ . The transmittance steadily rose as the temperature was increased between  $20^\circ\text{C}$  and  $50^\circ\text{C}$ , which may be because of the transition of larger size nanoaggregates of the added SAIL ([Gu][Ol]) to the smaller size nanoaggregates. At and above  $55^\circ\text{C}$ , the test material with a solid-like behaviour was converted to a semisolid-like material and showed non-flowing properties with a transmittance value of nearly 90% (Fig. 10). The transdermal patch with hydrogel-like properties was transformed into a transparent viscous solution with no fibrous aggregates when the temperature reached  $65^\circ\text{C}$  or higher. This was because of the breakdown of the hydrogen-bonding interactions responsible for the formation of the 3D network of PVA at high temperature.<sup>53</sup> These changes were reversible, as after cooling the system at room temperature, again the system turned opaque and solid.

The transdermal patch made up of pristine PVA (without the addition of [Gu][Ol]) had a low encapsulation efficiency (53%) and loading efficiency (3.2%). Whereas the transdermal patch containing [Gu][Ol] showed a greater encapsulation efficiency (65%) and loading efficiency (20.34%). This was because 5-FU has a tendency to form noncovalent interactions with [Gu][Ol], which we confirmed through comparative FTIR studies of [Gu][Ol] solution and 5-FU-added [Gu][Ol] solution. As demonstrated in Fig. 11, the OH stretching frequency in [Gu][Ol] at  $3441 \text{ cm}^{-1}$ , after the addition of 5-FU, was shifted to lower frequency, *i.e.*  $3400 \text{ cm}^{-1}$ . This indicated the formation of hydrogen bonds between the drug and the SAIL.

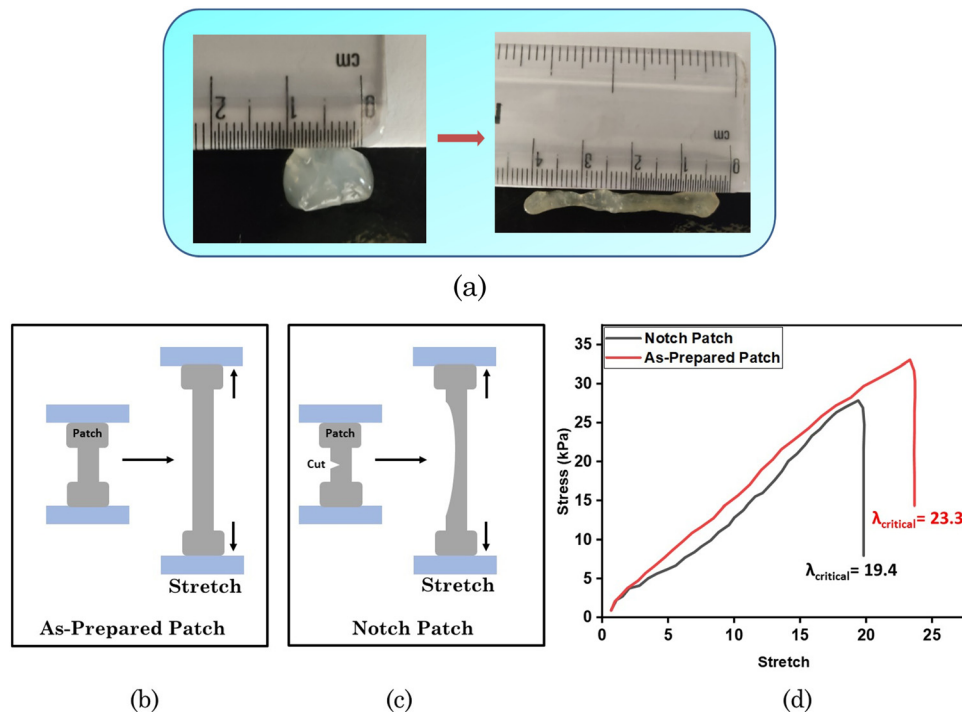


Fig. 7 (a) Visual images of stretchability. Graphical representation of the (b) as-prepared patch and (c) notched patch. (d) Stress–stretch curves of the notched patch and the as-prepared patch.

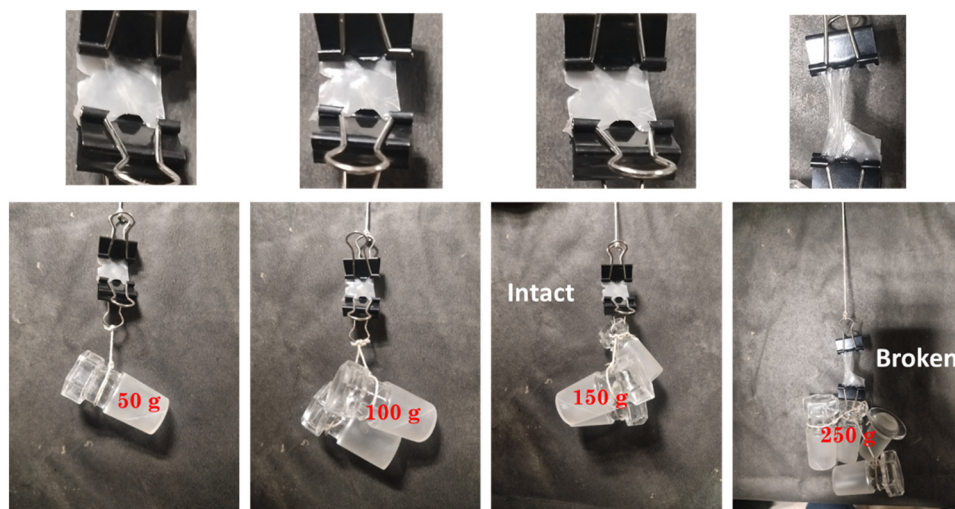


Fig. 8 Toughness study of the hydrogel patch.

SANS measurements were also performed for the 5-FU-loaded system and the experimental data were compared with the system without loading 5-FU (Fig. 12). Both the experimental data were best fitted using eqn (5). In the presence of 5-FU, the correlation length further decreased to 2.5 nm. The encapsulation of the drug in the [Gu][OI] aggregates embedded in the polymer gel matrix can increase the size of these aggregates, which in turn will further reduce the correlation length.

As the patch will be used to deliver a drug through penetrating the SC barrier of skin to the affected area, it was important to study the effect of the system on the SC. This was done by FTIR. FTIR studies of the SC were thus performed as described in the Materials and methods section to evaluate the effect of the investigated system on the structure and permeability of the SC. As shown in Fig. 13, the comparative IR spectra of the control and SC after incubation with the test material showed that the characteristic IR peaks of SC after incubating it with



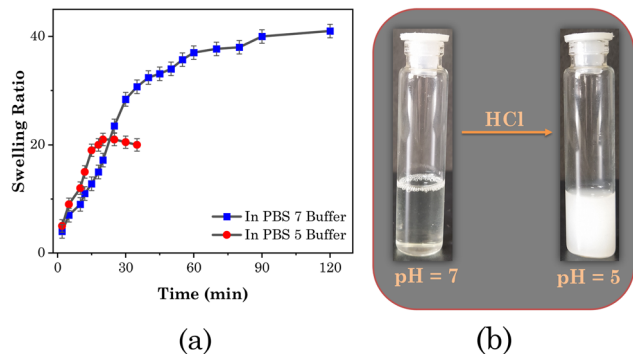


Fig. 9 (a) Swelling behaviour of the system at pH 5 (●) and pH 7 (■). (b) Visual images of the aqueous solution of [Gu][OI] at pH 7 and pH 5.

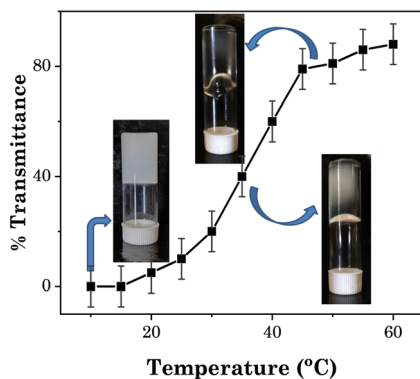


Fig. 10 Turbidity of the system as a function of temperature.

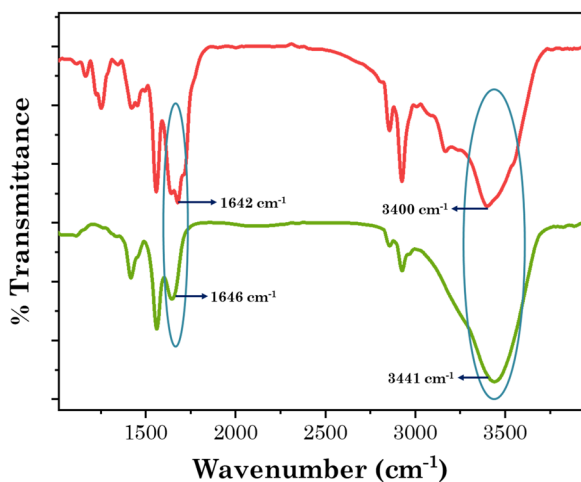


Fig. 11 Comparative FTIR spectra of [Gu][OI] (green) and [Gu][OI] + 5-FU (red).

the patch were slightly red-shifted compared to the control. The characteristic IR peaks for the lipid at 2849 cm<sup>-1</sup> (C-H symmetric vibration) and 2918 cm<sup>-1</sup> (C-H asymmetric vibration) were shifted to 2854 cm<sup>-1</sup> and 2923 cm<sup>-1</sup>, respectively. This shift in the IR peaks to higher wavenumbers indicated the

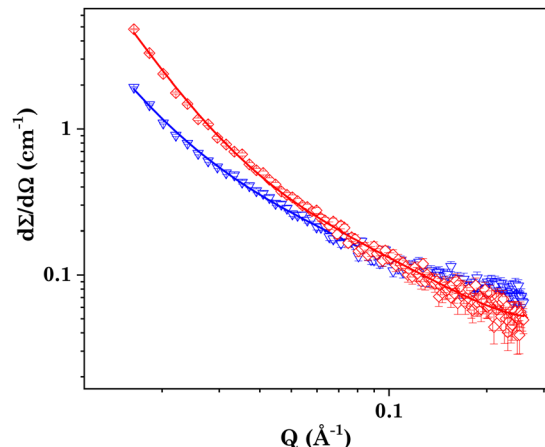


Fig. 12 SANS scattering of PVA + borax + [Gu][OI] (red) and PVA + borax + [Gu][OI] + 5-FU (blue).

transformation of the lipid form of the SC from an orthorhombic conformation to a liquid-crystalline manner, which is a more fluid structure.<sup>61</sup> Also, the characteristic peaks of keratin for the NH-C=O vibrations were also red-shifted from 1629 cm<sup>-1</sup> to 1632 cm<sup>-1</sup> and from 1538 cm<sup>-1</sup> to 1542 cm<sup>-1</sup>, respectively. This provides information regarding the structure of the proteins in the “horny layer” of the SC. It can be concluded from the spectra that the conformation of keratin turned to a random coil structure after incubation with the patch.

These results demonstrate the effect of the patch on the skin barrier properties and indicate that the transdermal patch was able to penetrate the SC, through disruption of the lipid bilayer packing and helical structure of keratin.<sup>21,62</sup> Further, two key factors of transdermal drug delivery that should be considered for the patch system are the enhancement ratio (ER) and irritation potential (IP). The ability of chemical penetration enhancers to enhance the penetration through the skin is known as the ER and the IP is assessed for considering the skin irritation potential of a system. The skin barrier disruption and ER value are predominantly correlated with the -CH<sub>2</sub>-

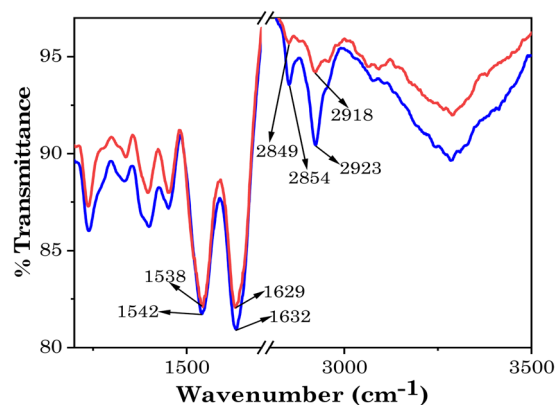


Fig. 13 FTIR spectra of SC before (red) and after (blue) treatment with the transdermal patch.



**Table 3** FTIR spectral shifts of the SC before and after treatment with gel

SC components	Stretching frequency	Before	After	$\Delta$ Shift
Lipid	CH <sub>2</sub> -asymm (cm <sup>-1</sup> )	2918	2923	5
	CH <sub>2</sub> -symm (cm <sup>-1</sup> )	2849	2854	5
Keratin	NH-C=O (cm <sup>-1</sup> )	1629	1632	3
		1538	1542	4

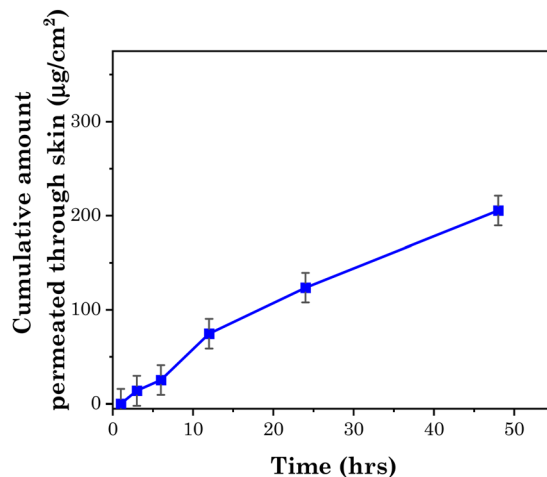
symm (cm<sup>-1</sup>) and IP is correlated with -NH-C=O (cm<sup>-1</sup>) groups.<sup>36</sup> As described in Table 3, for the studied transdermal patch, the -NH-C=O (cm<sup>-1</sup>) value was very low (*i.e.* 3 cm<sup>-1</sup>). This indicates the significant potency and safety of the designed transdermal patch as an ideal transdermal drug-delivery system.

To evaluate the safety profile of the prepared hydrogel patch, *in vitro* histological analysis was carried out (Fig. 14). The epidermis and dermis layers of the skin were well organized after treatment with PBS (control), as shown in Fig. 14(a). Further, the same kind of results were obtained even after treatment of the skin with the investigated system (Fig. 14(b)). *In vitro* histological analysis revealed no significant structural damage to the skin after being treated with the investigated system, which verified the biocompatibility of the prepared hydrogel patch.

### 3.1. Drug permeation study

5-FU is a hydrophilic polar drug that is highly resisted by the lipophilic components of the SC to inhibit its penetration in the skin. To enhance the penetration of 5-FU through skin, it is administered with chemical penetration enhancers. According to Dai *et al.*, the maximum permeation of 5-FU through skin is 9.72  $\mu\text{g cm}^{-2}$  without any additive. Dai *et al.* prepared four types of cocrystals of 5-FU with isomeric hydrobenzoic acid and salicylic acid, which enhanced the permeation of 5-FU up to 15.92  $\mu\text{g cm}^{-2}$  within 8 hours.<sup>63</sup> Rajinikanth *et al.* prepared a nanostructured lipid carrier-based hydrogel for the topical delivery of 5-FU, and the cumulative amount of drug penetrated from this system through the skin was 91.25  $\mu\text{g cm}^{-2}$  within 12 hours.<sup>64</sup>

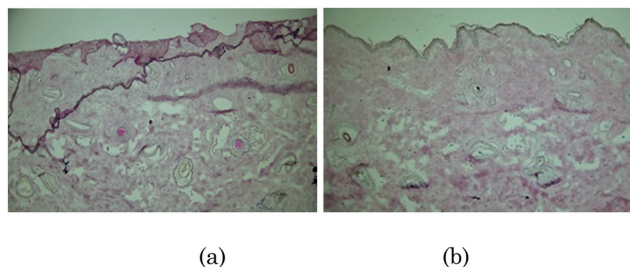
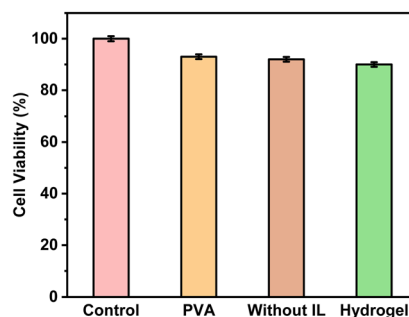
The studied transdermal patch enabled a high penetration of the drug, *i.e.* up to 280  $\mu\text{g cm}^{-2}$ . Moreover, the patch allowed the drug to penetrate through skin sustainably, as demonstrated in Fig. 15, which shows the rate of permeation of drug through goat skin as measured with the help of Franz diffusion

**Fig. 15** Transdermal permeation rate of 5-FU at pH 7.4.

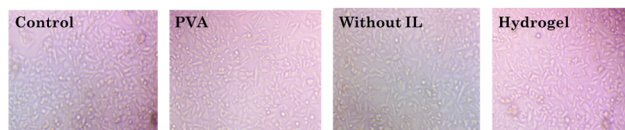
cell at pH 7.4. The amount of drug permeated through the skin at pH 7.4 was  $\sim 200 \mu\text{g cm}^{-2}$ , showing the high permeation rate of the drug through the skin. The reason for the enhanced penetration of the polar hydrophobic drug through the SC was as described *vide supra*, whereby guanidinium ions interact with the lipophilic anions of SC, which facilitates the translocation of the drug.<sup>54</sup>

### 3.2. Cell viability study with HaCaT and MCF 07 cell lines

We assessed the cytotoxicity of the transdermal patch against human breast cancer cells (MCF 07) as well as human keratinocyte cells (HaCaT), *i.e.* normal skin cells. For the HaCaT cell line, as exhibited in Fig. 16 and Table 4, the cell viability for PVA only was 93.79%, while for the hydrogel without [Gu][Ol] it was 92.92%, and for the hydrogel with [Gu][Ol] it was 90.90%. Hence, it could be concluded that the system had the least

**Fig. 14** *In vitro* histological evaluation of skin treated with (a) PBS (control) and (b) hydrogel patch.

(a)



(b)

**Fig. 16** (a) *In vitro* cell viability (HaCaT cell line) and (b) Microscopic images of the cell viability of different compositions of the test system.

**Table 4** Statistical data for the *in vitro* cell viability of the system

Compounds	Cell viability (%)	Average	SD
Control	100 99.52 100	99.98	0.1
PVA	93.92 95.52 91.93	93.79	0.3
Without IL	93.93 90.90 93.95	92.92	1.749
Hydrogel	90.90 91.92 89.90	90.90	0.2

toxicity for healthy skin cells. Further, we calculated the cell viability against the MCF-07 cell line with and without loading 5-FU through treating MCF-07 cell lines. As demonstrated in Fig. 16 and Table 5, the cell viability for the transdermal patch without loading 5-FU was found to be 81.9%, which may be because of the anticancer activity of guanidinium cations, as

**Table 5** Statistical data for the *in vitro* cell viability of the system

Compounds	Cell viability (%)	Average	SD
Control	100 99.85 100	99.95	0.08
System without 5-FU	81.93 81.75 82.02	81.90	0.13
System with 5-FU	24.71 24.90 24.58	24.73	0.16

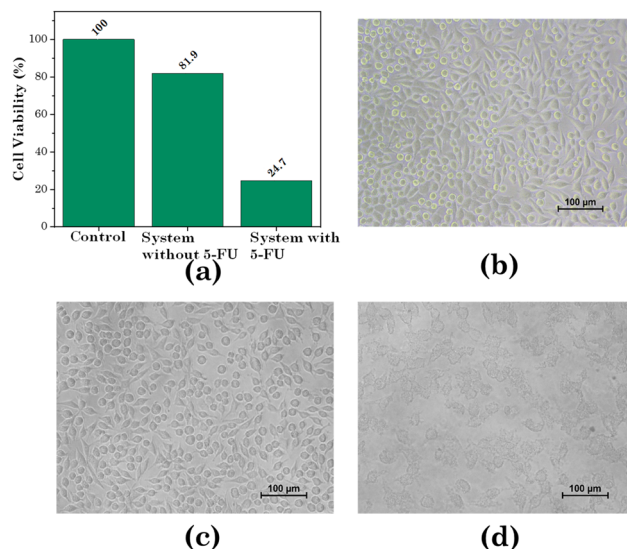


**Fig. 17** Cytotoxicity assay (a) cell viability of the MCF-07 cell line with the system, (b) microscopic image of the MCF-07 cell line before treatment, (c) microscopic image of the MCF-07 cell line after treatment with the system without loading 5-FU, (d) microscopic image of the MCF-07 cell line after treatment with the system loaded with 5-FU.

reported in the literature. For instance, Rothbard *et al.* explained the interaction of guanidinium with the lipid bilayer of cell membrane through H-bonding and emphasized the enhanced cellular uptake of guanidinium rich compounds.<sup>65</sup> Tay *et al.* reported that guanidinium-functionalized polycarboxylate, because of its high cellular uptake, could exert anticancer activity.<sup>66</sup> The cell viability of MCF-07 cells here decreased by ~24% within 24 h following the addition of the 5-FU-loaded system (Fig. 17). After adding 200 mg of test material to the culture media and as per the loading efficiency of transdermal patch, the calculated concentration of 5-FU added in the culture media was 29.21  $\mu\text{M}$ . The cell viability of MCF-07 cell lines at 30  $\mu\text{M}$  concentration of free 5-FU has already been reported to be ~27%.<sup>67</sup> However, for the test material with a 29.21  $\mu\text{M}$  concentration of 5-FU in combination with [Gu][OI], the cell viability was 24%, which was lower than that of free 5-FU. This suggests the improved efficacy of 5-FU when formulated in nanoaggregates of [Gu][OI].<sup>27</sup>

## 4. Conclusion

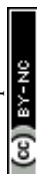
In this study, a novel transdermal patch based on PVA and borax was designed and prepared. The designed transdermal patch had moisture permeability, flexibility, biocompatibility, outstanding thermomechanical properties, recyclability, and adhesiveness. Also, due to the addition of borax it exhibited self-healing properties. The pH-responsive and permeation enhancer SAIL, *i.e.* [Gu][OI], was added to the patch and then the patch was loaded with the anticancer drug 5-FU. The 5-FU was encapsulated within the nanoaggregates of SAIL, as confirmed through SANS, showing these nanoaggregates of SAIL were entrapped within the aggregated 3D network of PVA and borax. Hence, the designed and prepared transdermal patch had excellent transdermal permeation and pH-responsive characteristics along with the desired mechanical properties. For the treatment of localized tumours, such as breast malignancy and skin malignancy, this designed transdermal patch can be a novel drug-delivery system, as it can deliver a drug through penetrating the skin, while enhancing the efficacy of the drug, reducing the required amount of drug, and most importantly reducing the side effects of the drug through the localized and targeted delivery of the drug.

## Conflicts of interest

The authors declare that they have no known competing financial interests or personal relationships that could have appeared to influence the work reported in this paper.

## Acknowledgements

NM acknowledges the financial assistance of UGC-DAE for the Collaborative Research Scheme (UDCSR/MUM/CRS-M-997/2023). The authors are thankful to Dr Arvind Kumar (CSMCRI, Bhavnagar) for useful discussion.



## References

- 1 V. Raviraj, B. T. T. Pham, B. J. Kim, N. T. H. Pham, L. F. Kok, N. Painter, N. C. Delic, S. K. Jones, B. S. Hawkett and J. G. Lyons, *Cancer Nanotechnol.*, 2021, **12**, 1–15.
- 2 R. Neupane, S. H. S. Boddu, M. S. Abou-Dahech, R. D. Bachu, D. Terrero, R. J. Babu and A. K. Tiwari, *Pharmaceutics*, 2021, **13**, 960.
- 3 M. R. Prausnitz and R. Langer, *Nat. Biotechnol.*, 2008, **26**, 1261–1268.
- 4 B. C. Palmer and L. A. DeLouise, *Molecules*, 2016, **21**, 7–9.
- 5 T. Jiang, G. Xu, G. Chen, Y. Zheng, B. He and Z. Gu, *Nano Res.*, 2020, **13**, 1810–1824.
- 6 V. Krishnan and S. Mitragotri, *Adv. Drug Delivery Rev.*, 2020, **153**, 87–108.
- 7 C. Dianzani, G. P. Zara, G. Maina, P. Pettazzoni, S. Pizzimenti, F. Rossi, C. L. Gigliotti, E. S. Ciamporcerio, M. Daga and G. Barrera, *BioMed Res. Int.*, 2014, **2014**, 895986.
- 8 Y. L. Lin, C. H. Chen, H. Y. Wu, N. M. Tsai, T. Y. Jian, Y. C. Chang, C. H. Lin, C. H. Wu, F. T. Hsu, T. K. Leung and K. W. Liao, *J. Nanobiotechnol.*, 2016, **14**, 1–10.
- 9 C. Gorzelanny, C. Mess, S. W. Schneider, V. Huck and J. M. Brandner, *Pharmaceutics*, 2020, **12**, 1–31.
- 10 M. R. Chowdhury, R. M. Moshikur, R. Wakabayashi, M. Moniruzzaman and M. Goto, *Int. J. Pharm.*, 2021, **601**, 120582.
- 11 S. Kozaka, Y. Tahara, R. Wakabayashi, T. Nakata, T. Ueda, N. Kamiya and M. Goto, *Mol. Pharmacol.*, 2020, **17**, 645–655.
- 12 R. Wakabayashi, H. Kono, S. Kozaka, Y. Tahara, N. Kamiya and M. Goto, *ACS Biomater. Sci. Eng.*, 2019, **5**, 2297–2306.
- 13 B. Lu, Y. Bo, M. Yi, Z. Wang, J. Zhang, Z. Zhu, Y. Zhao and J. Zhang, *Adv. Funct. Mater.*, 2021, **31**, 1–12.
- 14 V. Sugumar, M. Hayyan, P. Madhavan, W. F. Wong and C. Y. Looi, *Biomedicines*, 2023, **11**, 664.
- 15 P. Karande and S. Mitragotri, *Biochim. Biophys. Acta, Biomembr.*, 2009, **1788**, 2362–2373.
- 16 I. B. Pathan and C. M. Setty, *Trop. J. Pharm. Res.*, 2009, **8**, 173–179.
- 17 B. Lu, T. Liu, H. Wang, C. Wu, H. Chen, Z. Liu and J. Zhang, *J. Mol. Liq.*, 2022, **351**, 118643.
- 18 S. N. Pedro, C. S. R. Freire, A. J. D. Silvestre and M. G. Freire, *Int. J. Mol. Sci.*, 2020, **21**, 1–50.
- 19 W. Wilms, M. Wozniak-Karczewska, A. Syguda, M. Niemczak, Ł. Ławniczak, J. Pernak, R. D. Rogers and Ł. Chrzanowski, *J. Agric. Food Chem.*, 2020, **68**, 10456–10488.
- 20 J. M. Gomes, S. S. Silva and R. L. Reis, *Chem. Soc. Rev.*, 2019, **48**, 4317–4335.
- 21 S. Uddin, M. R. Islam, M. R. Chowdhury, R. Wakabayashi, N. Kamiya, M. Moniruzzaman and M. Goto, *ACS Appl. Bio Mater.*, 2021, **4**, 6256–6267.
- 22 A. Pratap Singh, D. Sithambaram, R. Sanghavi, P. Kumar Gupta, R. Shanker Verma, M. Doble, R. L. Gardas and S. Senapati, *New J. Chem.*, 2017, **41**, 12268–12277.
- 23 S. Panda, K. Kundu, A. Basaiahgari, A. P. Singh, S. Senapati and R. L. Gardas, *New J. Chem.*, 2018, **42**, 7105–7118.
- 24 M. Karimi, A. Ghasemi, P. Sahandi Zangabad, R. Rahighi, S. M. Moosavi Basri, H. Mirshekari, M. Amiri, Z. Shafaei Pishabad, A. Aslani, M. Bozorgomid, D. Ghosh, A. Beyzavi, A. Vaseghi, A. R. Aref, L. Haghani, S. Bahrami and M. R. Hamblin, *Chem. Soc. Rev.*, 2016, **45**, 1457–1501.
- 25 H. Wang, L. Gao, T. Fan, C. Zhang, B. Zhang, O. A. Al-Hartomy, A. Al-Ghamdi, S. Wageh, M. Qiu and H. Zhang, *ACS Appl. Mater. Interfaces*, 2021, **13**, 54621–54647.
- 26 M. Jain, O. El Seoud, S. K. Kailasa and N. I. Malek, *J. Ion. Liq.*, 2022, **2**, 100046.
- 27 S. Tampucci, L. Guazzelli, S. Burgalassi, S. Carpi, P. Chetoni, A. Mezzetta, P. Nieri, B. Polini, C. S. Pomelli, E. Terreni and D. Monti, *Pharmaceutics*, 2020, **12**, 1–22.
- 28 H. Wang, B. Tan, J. Wang, Z. Li and S. Zhang, *Langmuir*, 2014, **30**, 3971–3978.
- 29 J. Cui, Y. Li, D. Chen, T. G. Zhan and K. D. Zhang, *Adv. Funct. Mater.*, 2020, **2005522**, 1–30.
- 30 Z. Yan, C. Dai, M. Zhao, Y. Li, M. Du and D. Peng, *Colloid Polym. Sci.*, 2015, **293**, 1759–1766.
- 31 R. Md Moshikur, M. R. Chowdhury, H. Fujisawa, R. Wakabayashi, M. Moniruzzaman and M. Goto, *ACS Sustainable Chem. Eng.*, 2020, **8**, 13660–13671.
- 32 M. R. Islam, M. R. Chowdhury, R. Wakabayashi, Y. Tahara, N. Kamiya, M. Moniruzzaman and M. Goto, *Int. J. Pharm.*, 2020, **582**, 119335.
- 33 M. Jain, S. Kumar, V. K. Aswal, A. Al-Ghamdi, S. Kumar Kailasa and N. I. Malek, *J. Mol. Liq.*, 2022, **360**, 119517.
- 34 C. L. Hannon and E. V. Anslyn, *Bioorg. Chem. Front.*, 1993, **3**, 193–255.
- 35 P. A. Wender, W. C. Galliher, E. A. Goun, L. R. Jones and T. H. Pillow, *Adv. Drug Delivery Rev.*, 2008, **60**, 452–472.
- 36 P. Karande, A. Jain, K. Ergun, V. Kispersky and S. Mitragotri, *Proc. Natl. Acad. Sci. U. S. A.*, 2005, **102**, 4688–4693.
- 37 M. A. Safwat, G. M. Soliman, D. Sayed and M. A. Attia, *Mol. Pharmaceutics*, 2018, **15**, 2194–2205.
- 38 P. Guo, C. Pi, S. Zhao, S. Fu, H. Yang, X. Zheng, X. Zhang, L. Zhao and Y. Wei, *Expert Opin. Drug Delivery*, 2020, **17**, 1473–1484.
- 39 T. S. Anirudhan, A. S. Nair and S. J. Bino, *Carbohydr. Polym.*, 2017, **173**, 131–142.
- 40 D. Singh, M. Pradhan, M. Nag and M. R. Singh, *Artif. Cells, Nanomed., Biotechnol.*, 2015, **43**, 282–290.
- 41 D. Bird and N. M. Ravindra, *Med. Devices Sens.*, 2020, **3**, e10069.
- 42 R. Md Moshikur, I. M. Shimul, S. Uddin, R. Wakabayashi, M. Moniruzzaman and M. Goto, *ACS Appl. Mater. Interfaces*, 2022, **14**, 55332–55341.
- 43 Y. W. Naguib, A. Kumar and Z. Cui, *Acta Pharm. Sin. B*, 2014, **4**, 94–99.
- 44 R. Neupane, S. H. S. Boddu, M. S. Abou-Dahech, R. D. Bachu, D. Terrero, R. J. Babu and A. K. Tiwari, *Pharmaceutics*, 2021, **13**, 960.
- 45 S. Kim, C. M. Day, Y. Song, A. Holmes and S. Garg, *Pharmaceutics*, 2023, **15**, 2577.
- 46 S. Singh, P. Singh, N. Mishra, P. Maurya, N. Singh, R. Nisha and S. A. Saraf, *Advanced Drug Delivery Systems in the Management of Cancer*, Elsevier, 2021, pp. 107–126.
- 47 D. B. Longley, D. P. Harkin and P. G. Johnston, *Nat. Rev. Cancer*, 2003, **3**, 330–338.



- 48 B. N. Singh and S. B. Jayaswal, *Drug Discoveries Ther.*, 2008, **2**, 128–135.
- 49 S. P. Cannavò, F. Guarneri, R. Giuffrida, E. Aragona and C. Guarneri, *Skin Res. Technol.*, 2017, **23**, 41–47.
- 50 V. Ramkumar and R. L. Gardas, *Cryst. Growth Des.*, 2022, **22**(6), 3646–3655.
- 51 A. H. Rantamäki, S. K. Ruokonen, E. Sklavounos, L. Kyllönen, A. W. T. King and S. K. Wiedmer, *Sci. Rep.*, 2017, **7**, 1–12.
- 52 J. S. Kwon, D. Y. Kim, H. W. Seo, S. H. Jeong, J. H. Kim and M. S. Kim, *Tissue Eng. Regen. Med.*, 2014, **11**, 211–216.
- 53 C. Wang, Z. Shen, P. Hu, T. Wang, X. Zhang, L. Liang, J. Bai and C. Wang, *J. Sol-Gel Sci. Technol.*, 2022, **101**, 103–113, DOI: [10.1007/s10971-021-05584-0](https://doi.org/10.1007/s10971-021-05584-0).
- 54 E. Wexselblatt, J. D. Esko and Y. Tor, *J. Org. Chem.*, 2014, **79**, 6766–6774.
- 55 R. Gupta, B. S. Dwadasi, B. Rai and S. Mitragotri, *Sci. Rep.*, 2019, **9**, 1–11.
- 56 M. Shibayama, *Soft Matter*, 2012, **8**, 8030–8038.
- 57 L. Valencia, E. M. Nomena, S. Monti, W. Rosas-Arbelaiz, A. P. Mathew, S. Kumar and K. P. Velikov, *Nanoscale*, 2020, **12**, 15652–15662.
- 58 J. Y. Kim, J. Y. Song, E. J. Lee and S. K. Park, *Colloid Polym. Sci.*, 2003, **281**, 614–623.
- 59 S. B. Ross-Murphy, *J. Texture Stud.*, 1995, **26**, 391–400.
- 60 Z. Wang, J. Chen, L. Wang, G. Gao, Y. Zhou, R. Wang, T. Xu, J. Yin and J. Fu, *J. Mater. Chem. B*, 2019, **7**, 24–29.
- 61 C. Wang, J. Zhu, D. Zhang, Y. Yang, L. Zheng, Y. Qu, X. Yang and X. Cui, *Int. J. Pharm.*, 2018, **535**, 120–131.
- 62 Y. Pyatski, C. R. Flach and R. Mendelsohn, *Biochim. Biophys. Acta, Biomembr.*, 2020, **1862**, 183335.
- 63 X. L. Dai, A. P. Voronin, W. Gao, G. L. Perlovich, T. B. Lu and J. M. Chen, *CrystEngComm*, 2019, **21**, 5095–5105.
- 64 P. S. Rajinikanth and J. Chellian, *Int. J. Nanomed.*, 2016, **11**, 5067–5077.
- 65 J. B. Rothbard, T. C. Jessop and P. A. Wender, *Adv. Drug Delivery Rev.*, 2005, **57**, 495–504.
- 66 J. Tay, Y. Zhao, J. L. Hedrick and Y. Y. Yang, *Theranostics*, 2021, **11**, 8977–8992.
- 67 J. A. Marchal, H. Boulaiz, I. Suárez, E. Saniger, J. Campos, E. Carrillo, J. Prados, M. A. Gallo, A. Espinosa and A. Aránega, *Invest. New Drugs*, 2004, **22**, 379–389.

